The Astronomical Journal, 168:39 (15pp), 2024 July https://doi.org/10.3847/1538-3881/ad4a74

Antenna Design for Absolute Sky Measurements at Gigahertz Frequencies—a First Step toward Detecting CMB Spectral Distortions from Recombination

Keerthipriya Sathish[1,2], Mayuri Sathyanarayana Rao[1], and Debdeep Sarkar[2]
[1] Raman Research Institute, C.V. Raman Avenue, Sadashivanagar, Bengaluru, 560080, India
[2] Department of Electrical Communication Engineering, Indian Institute of Science, C.V. Raman Road, Bengaluru, 560012, India
Received 2024 February 5; revised 2024 April 25; accepted 2024 May 9; published 2024 June 28

Abstract

There exist inevitable deviations in the cosmic microwave background spectrum from that of a blackbody. The additive distortions from photons emitted over the epoch of recombination are one such deviation. We present a novel scalable broadband antenna design motivated by detecting these spectral distortions in the 2.5–4 GHz band. This antenna is capable of maintaining the spectral quality of the measured sky spectrum to 1 part in 10^3 over the full band and outperforms conventional broadband antennas by at least an order of magnitude. While this is not sufficient to make a direct detection of the cosmological recombination radiation, it meets the baseline design criteria for an experiment that can make an absolute measurement of the sky spectrum at the millikelvin level, thereby making it capable of improving foreground models to global signal detection experiments (including those from cosmic dawn and the epoch of reionization) and addressing the problem of the excess radio background at 3.3 GHz reported by the ARCADE2 experiment.

Unified Astronomy Thesaurus concepts: Radio receivers (1355); Radio astronomy (1338); Radio telescopes (1360); Ground telescopes (687); Ground-based astronomy (686); Cosmology (343); Recombination (cosmology) (1365); Reionization (1383)

1. Introduction

The cosmic microwave background (CMB), a relic radiation from the early Universe, serves as a critical source of information in understanding the evolution and composition of our Universe. The CMB has a near-Planckian spectrum, corresponding to a blackbody of temperature 2.72548 ± 0.00057 K (Fixsen 2009). The measurement of this spectrum to 1 part in 10^5 is in itself a technical feat. However, this comes from data that are now over 25 yr old, from the FIRAS experiment on board the COBE satellite (Mather et al. 1999). Theoretical predictions posit the presence of inevitable faint deviations in the CMB spectrum from that of a blackbody. These are referred to as "spectral distortions" and arise from various processes of energy injection in the early Universe after the CMB has thermalized to a blackbody. For more details on the CMB thermalization and spectral distortions, we refer the reader to Sunyaev & Chluba (2009).

One such spectral distortion is the cosmological recombination radiation (CRR), which arises from the epoch of recombination (ERA). This epoch is marked by an extended period over which cosmological expansion and cooling caused the Universe to transition from a fully ionized primordial plasma to a gas of almost completely neutral hydrogen and helium atoms. The photons that are emitted during this period result in recombination lines that form an additive distortion to the underlying CMB spectrum and are an inevitable prediction of standard cosmology. The recombination lines are quasi-periodic ripples spanning a broad frequency range from 100 MHz to 3 THz, with an amplitude of ∼10 nK in the 2–6 GHz band, which is estimated to have the highest signal-to-noise ratio (S/N) for ground-based detection (Rao et al. 2015).

Henceforth, we refer to this as the ERA signal. Detecting and precisely measuring the ERA signal can help us understand the thermal history of the Universe, detect any exotic energy mechanisms of energy injection, improve the constraints on the CMB's average monopole temperature over the sky, and provide a direct experimental method to measure the abundance of helium in the early Universe before the formation of the first stars (Sunyaev & Chluba 2009). Figure 1 shows the expected additive intensity to the CMB due to the ERA signal over a wide band spanning ∼100 MHz–3 THz, as predicted by CosmoSpec (Chluba & Ali–Haimoud 2016). The equivalent baseline-subtracted Rayleigh–Jeans temperature from the ERA signal in the 2–6 GHz band is shown in Figure 2.

This ERA signal is a global or all-sky signal and is unpolarized. It can be detected by measuring the absolute temperature of the sky at different frequencies. However, radiation from our own Galaxy, extragalactic radiation, and atmospheric noise, in addition to the CMB, form natural foreground contaminants to signal detection. The foreground signal is 8 orders of magnitude brighter than the ERA signal even in the highest-S/N window of 2–6 GHz, and its removal is essential to detect the ERA signal. Other astrophysical phenomena do not replicate the distinctive shape of the predicted ERA signal, and hence the two can be separated in an ideal observation. In addition to the foreground contaminants, the ERA signal can be obscured or distorted by instrumental systematics arising from various sources like uncalibrated gain in the receiver bandpass, sinusoidal ripples caused by impedance mismatches, antenna sidelobes, chromaticity in the main lobe, and any noise in the system that does not average below signal levels with time. Overcoming these instrumental chromatic effects is essential for precise measurements.

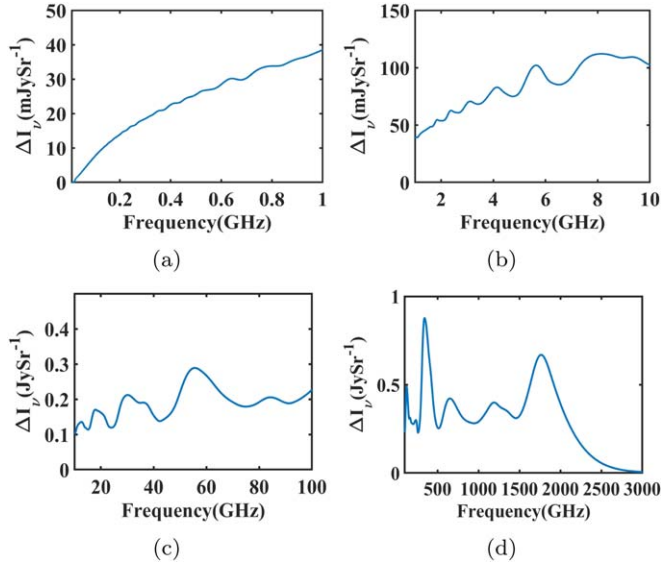

Figure 1. The additive spectral structure expected in the intensity of the CMB radiation, due to the cosmological recombination of hydrogen and helium (Chluba & Sunyaev 2006, 2007; Rubiño-Martín et al. 2006). The wide frequency range is successively covered in four panels. (a) Frequency range between 0.1 and 1 GHz. (b) Frequency range between 1 and 10 GHz. (c) Frequency range between 10 and 100 GHz. (d) Frequency range between 100 GHz and 3 THz. Signal prediction from CosmoSpec (Chluba & Ali–Haimoud 2016).

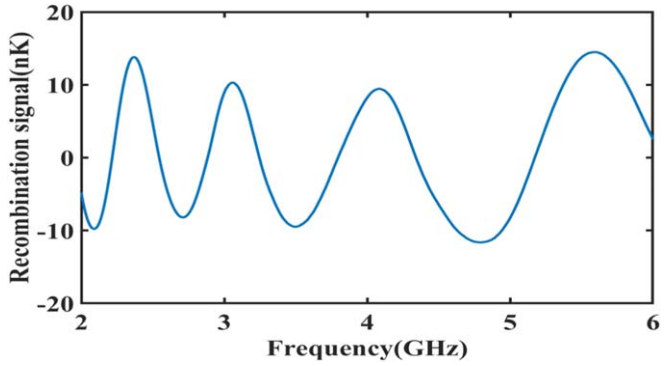

Figure 2. ERA signal expected to be detected as residuals in the 2–6 GHz band (Rao et al. 2015), after removing the smooth component when embedded in the sky spectrum received by an ideal antenna and receiver.

At the forefront of CMB distortion research, several balloon- and space-based experiments focused on spectral distortions from the early Universe have been proposed. Notable examples include the following: PIXIE covers the frequency range of 15 GHz–3 THz (Kogut et al. 2011, 2016; Chluba et al. 2021; Maffei et al. 2023), with the capability of measuring polarization information. Super-PIXIE (Kogut et al. 2019) is proposed with enhanced sensitivity, operating from 10 GHz to 6 THz. Furthermore, Voyage 2050 (Chluba et al. 2021) has been proposed to exceed the sensitivity of Super-PIXIE, while Voyage 2050+ is anticipated to surpass Voyage 2050 in sensitivity. The balloon-based experiment BISOU (Maffei et al. 2023) has been proposed as a pathfinder to future space-based CMB spectral distortion missions. The article by Hart et al. (2020) delves into the sensitivity requirements for some of these remarkable space-based experiments, each contributing to our understanding of the early Universe.

Specifically toward detecting the CRR, two prominent experiments have been proposed. The first is APSERa (Rao et al. 2015), a ground-based experiment in the 2–6 GHz band, wherein the antenna designed in this article finds application. The second is a space-based experiment proposed by Desjacques et al. (2015), covering a range of 30–600 GHz. While Rao et al. (2015) present a feasibility study for a ground-based discussion of the ERA (the baseline-subtracted signal over 2–6 GHz) signal, an *nK* signal detection is a challenging problem requiring careful design and characterization of every single aspect of the experiment. In this paper, we focus on the antenna design of such an experiment. Our interest in the antenna design is twofold. First, the antenna is a critical first step to signal detection, forming the sensing element of the radiometer. Second, the guidelines for designing an antenna to detect the ERA signal are very similar to yet another wide and faint global cosmological signal, namely that arising from the global redshifted 21 cm signal from cosmic dawn (CD) and the epoch of reionization (EoR).

The rest of the paper is structured as follows: Section 2 presents a guideline for good practices in antenna design for the ERA signal, with several parallels to the antenna design for CD and EoR signal. Section 3 presents a pipeline to qualify the antenna's performance using a simulated sky model. Section 4 presents a comparison of the performance of conventional ultra-wideband (UWB) antennas. Section 5 describes the design of the novel dual-polarized fantail antenna following the design guidelines listed in Section 2. Section 6 presents a comprehensive characterization of the same. Lastly, Section 7 summarizes our findings and proposes directions for future research.

2. Antenna Design Guidelines for Detecting Broad CMB Spectral Distortions

The fundamental natural challenge for experiments seeking to detect global cosmological signals—CD, EoR, and ERA signals—is the bright emission from Galactic synchrotron radiation and the CMB itself, in addition to cosmic dust emission, free electron emission, and emission from Galactic and extragalactic bright sources. The foregrounds can be 10^6–10^9 times brighter than the cosmological signal. While it is challenging, there exist methods suggested in the literature to exploit intrinsic differences between the foregrounds and the cosmological signals. These include using the spectral features (foregrounds are smooth as opposed to spectrally complex signals; Rao et al. 2017; Bevins et al. 2021) and polarization and time variability (foregrounds are polarized and vary, whereas the global signal is unpolarized and constant; Switzer & Liu 2014; Nhan et al. 2017; Tauscher et al. 2020).

We adopt the first approach, namely exploiting differences in the spectral complexity between the ERA signal and foregrounds, as the basis for antenna design. The foreground separation approach and antenna design are intimately related, as the antenna forms the first element of any radiometer and imprints its properties on the observed measurement—including the foregrounds and cosmological signal.

Generally, antenna properties, such as the beam pattern, reflectance, and overall efficiency, exhibit variability across the frequency band. Therefore, it is essential to ensure that the antenna does not introduce any spurious spectral structure in the data, which results in artifacts that mimic the cosmological signal. That is, it is important to ensure that the antenna does

not introduce any spectral features from beam chromaticity or coupling to the receiver, which hinder the signal separation from foregrounds. Various global experiments in the more mature field of global 21 cm cosmology seeking to detect the signal from CD and EoR have adopted diverse approaches in antenna design and sensitivity validation. For instance, experiments like EDGES (Bowman et al. 2018; Mahesh et al. 2021), SARAS (Singh et al. 2022), and REACH (Cumner et al. 2022) utilize single-antenna telescopes or radiometers, focusing on detecting the global EoR signal. Each of these experiments employs unique strategies in antenna design, system configuration, and data analysis techniques for foreground subtraction and system calibration. Any experiment, targeting the even fainter ERA signal, will encounter similar challenges with tighter tolerances. However, the antenna design principles translate well between CD, EoR, and ERA signal detection experiments. The following are some properties of an antenna that are conducive to signal detection:

1. *Wide beamwidth*: By definition, the global or monopole spectral distortion of the CMB spectrum is observable across the entire sky, and not preferentially from any specific direction. Thus, an antenna with a wide beam is preferable to increase the collecting area of radiation.
2. *Achromatic beam*: The sky signal enters the receiver chain electronics after convolution with the antenna's beam pattern. Therefore, variations in the antenna beam pattern with frequency result in the sky being weighed differently at different frequencies. This phenomenon is denoted as the "mode-mixing" problem (Bowman et al. 2009; Thyagarajan et al. 2016; Morales et al. 2012). A key approach to mitigate this issue is to have antenna beam patterns with minimal chromaticity, a main lobe with no ripples, and minimal sidelobes.
3. *Smooth return loss*: The sky signal after being convolved with the antenna's beam is scaled by the antenna's reflection efficiency before entering the receiver electronics. Spectral richness in the return loss, like ripples, resonance dips, and inflections, introduces spectral structure in the observed sky spectrum, complicating foreground and cosmological signal separation. Hence, it is necessary to have the antenna's return loss exhibit a smooth variation with frequency. The mathematical definition of smoothness in this context is presented in Section 3. The foregrounds are expected to be smooth, but they can also exhibit spectral curvature due to physically motivated processes; therefore, one inflection or turning point in the in-band return loss is acceptable.
4. *Minimal back lobes*: In the conventional setup of an antenna positioned above a ground plate on soil, the primary beam of the antenna convolves with the sky, while the back lobe convolves with the ground surface. The effects of antenna coupling with the local environment, such as with objects in the horizon and the soil, have been discussed in the literature in the context of experiments aimed to detect global redshifted 21 cm signal from CD (Bennett et al. 2013; Pattison et al. 2023). However, our investigations in the current work are limited to the effects of sky and soil. The overall temperature of the sky, including atmospheric contributions, is anticipated to be on the $\mathcal{O}(10)$K in the gigahertz frequency range. In contrast, the temperature of the soil is expected to be $\mathcal{O}(300)$ K. The total antenna temperature is the summation of the contributions of both the sky and soil convolutions with the antenna pattern. Therefore, the antenna must have minimal power radiated in the back lobes, to minimize the impact of radiation from the ground (soil) below. Thus, a high front-to-back ratio is required, with minimal back lobes and finite ground plate to increase the sensitivity of our system toward sky.
5. *Dual polarization*: The global CMB spectral distortion signals, like the EoR signal and ERA signal, are expected to be unpolarized, differentiating them from the polarized foreground. This inherent dissimilarity can aid in the decoupling of the signal from foregrounds, motivating the use of dual-polarized antennas.

In this work we explore the antenna designs for detecting the signals from the ERA. Therefore, the design criteria outlined above must be met across a sufficiently wide bandwidth over which the ERA signal has multiple turning points or inflections to effectively separate the signal from the smooth foreground component. While an octave bandwidth in the high-S/N region of 2–6 GHz is desirable, we place a requirement of at least three turning points in the band. This signal prediction is derived from CosmoSpec (Chluba & Ali–Haimoud 2016) employing the Planck Lambda cold dark matter cosmology, which suggests the presence of multiple turning points within the 2–6 GHz band. The frequency range of 2.5–4 GHz meets this criterion and is the band of operation for the antenna presented in this article.

We recognize that designing an antenna that is sensitive (in spectral complexity) to a signal that is *nK* in amplitude is a daunting task. Herein, we take a first step in achieving an order-of-magnitude improvement over conventional broadband antennas. The resulting novel scalable wideband fantail antenna can find application in making a high-precision absolute measurement of the gigahertz radio sky. The TRIS radiometer observed the sky at spot frequencies of 0.6, 0.82, and 2.5 GHz (Zannoni et al. 2008). This resulted in useful constraints for CMB spectral distortions, including new limits on the free–free spectral distortion $-6.3\times10^{-6}<Y_{ff}<12.6\times10^{-6}$ and improving the upper limit on the chemical potential distortion $|\mu|<6\times10^{-5}$ (Gervasi et al. 2008). Yet another absolute sky temperature measurement was ARCADE-2, which reported the presence of a radio excess at 3.3 GHz (Fixsen et al. 2011). This result has elicited great interest among astronomers. Explanations range from possible unresolved extragalactic point sources (Condon et al. 2012; Vernstrom et al. 2014, 2011) to annihilating dark matter (Fornengo et al. 2011; Hooper et al. 2012; Fang & Linden 2015). A comprehensive discussion is presented in Singal et al. (2018). There is also contention on whether reported radio excess is real in Subrahmanyan & Cowsik (2013). A broadband absolute sky measurement (as opposed to spot frequency measurement) of the gigahertz radio sky can prove to be extremely useful, in improving limits on CMB spectral distortions; improving foreground maps for CD, EoR, and ERA signals; and addressing the mystery of the excess radio background.

In keeping with the design guidelines listed above, we present a highly frequency-independent, broadband, dual-polarized fantail antenna. With a self-calibrated cryogenically cooled receiver, the antenna presented herein will be capable of making an absolute measurement of the radio sky over 2.5–4 GHz to 1 part in 10^3.

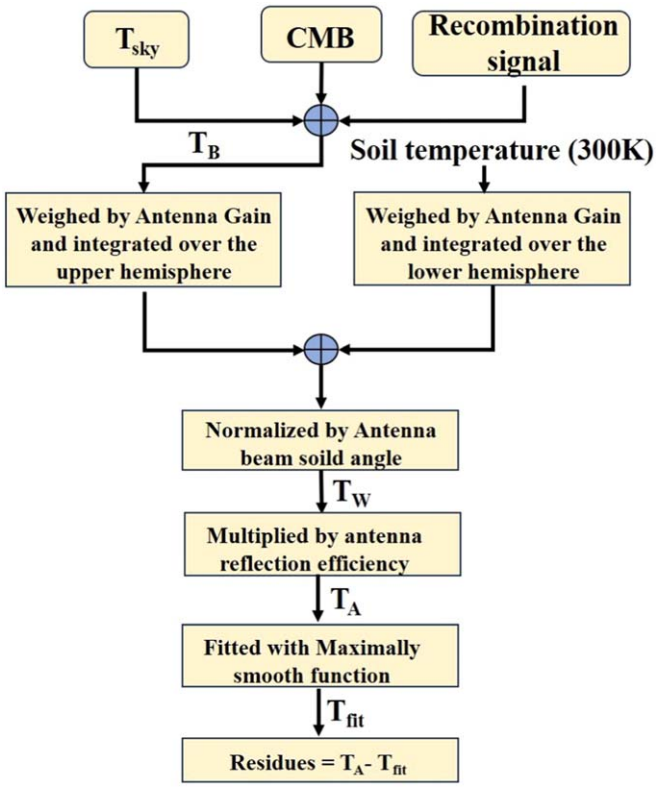

Figure 3. Flowchart of the antenna validation pipeline through which the antenna's chromaticity and consequently its suitability for ERA signal detection are quantified ($T_{\rm sky}$—sky temperature; CMB—cosmic microwave background).

3. Antenna Validation Pipeline

The design criteria described in Section 2 are guidelines for antennas detecting global cosmological spectral signatures. Conventional software simulations do not readily present a metric to evaluate the performance of antennas for such an application. To effectively assess an antenna's suitability for an ERA signal detection experiment, a custom antenna validation software pipeline has been developed.

The antenna validation pipeline convolves the antenna's radiation pattern with a model of the radio sky. The sky-convolved signal is then passed through the antenna's return loss function to generate a mock-sky spectrum as would be recorded by a bandpass-calibrated receiver. One can generate two classes of realizations of the mock spectra: (1) where the ERA signal is present as an additive component to the sky model, and (2) the null hypothesis case, where the ERA signal is absent. The ability to distinguish the presence of the ERA signal from the null hypothesis case is a key measure of antenna performance. The pipeline is versatile and can be modified to use different sky models, realizations of the cosmological signal, antenna radiation pattern, and return loss. A flowchart description of the pipeline is given in Figure 3.

There exist several sky models, such as GSM (de Oliveira-Costa et al. 2008) and GMOSS (Rao et al. 2016). Using existing all-sky maps at spot frequencies, these models generate sky maps at desired frequencies using data-driven interpolation or physically motivated analytical functions. The sky maps thus generated can be used as an input to the pipeline for convolution with the antenna beam. The errors that result from interpolation methods used in these sky models can become a limiting factor in analyzing antenna behavior. Thus, we have made the deliberate choice of using a power-law function as a sky model to generate maps that are input to the pipeline for the results presented in this paper. The power-law emission is physically motivated, as the dominant radiative process is the synchrotron emission from the acceleration of cosmic electrons along magnetic field lines in our Galaxy, which has a power-law form. This, in addition to the CMB itself over the frequency range of interest, is the dominant foreground signal. We use three maps at 408 MHz (Haslam et al. 1982), 1420 MHz (Reich 1982; Reich & Reich 1986), and 23 GHz from the WMAP Science Team (Bennett et al. 2013), with appropriate scaling and offset corrections, in the HEALPIX (Gorski et al. 2005) formalism. With a pixel resolution corresponding to $\sim 3\overset{\circ}{.}7$, we describe Galactic emission from each pixel using

$$T_{\rm sky}(l,\, b,\, \nu) = T_{l,b,408}\left(\frac{\nu}{408}\right)^{\alpha(l,b)}, \tag{1}$$

where $T_{\rm sky}$ is the sky temperature at frequency ν and at Galactic latitude and longitude of $(l,\, b)$. $T_{l,b,408}$ is the temperature at a pixel with coordinates $(l,\, b)$ in the 408 MHz sky map, where the spectral index $\alpha(l,\, b)$ is determined by fitting a power law between the values in the three raw maps, namely 408 MHz, 1420 MHz, and 23 GHz.

The input to the pipeline is the total brightness temperature of the sky T_B. It is the summation of the Galactic emission in Equation (1) and the CMB radiation. The summation is done in intensity units and converted to equivalent temperature using the Rayleigh–Jeans approximation.

Given the temporal variability of the sky, T_B is a function of angles $(\theta,\, \phi)$, frequency (ν), and time (t). This sky temperature undergoes weighting by the antenna's gain $G(\theta,\, \phi,\, \nu)$, integrated across the upper hemisphere. Sky emission in Galactic coordinates $(l,\, b)$ is converted to the antenna coordinate system or horizontal coordinates $(\theta,\, \phi)$ using standard formulae and depends on the observing location of the antenna on Earth and local time. The lower hemisphere of the antenna's gain is weighted by a constant soil temperature of 300 K, as illustrated in Equation (2). The outcome of this beam-weighting process results in a spectrum referred to as $T_W(\nu,\, t)$ given in Equation (3). This T_W spectrum is then subject to multiplication by the antenna's reflection efficiency (Γ, reflection coefficient), as indicated in Equation (4). The resulting spectrum, $T_A(\nu,\, t)$, is the measured mock-sky spectrum:

$$\begin{aligned} T_V(\nu,\, t) = &\int_0^{2\pi}\int_0^{\frac{\pi}{2}} T_B(\theta,\, \varphi,\, \nu,\, t) * G(\theta,\, \varphi,\, \nu)\sin\theta d\theta d\varphi \\ &+ \int_0^{2\pi}\int_{\frac{\pi}{2}}^{\pi} 300 * G(\theta,\, \varphi,\, \nu)\sin\theta d\theta d\varphi \end{aligned} \tag{2}$$

$$T_W(\nu,\, t) = \frac{T_V(\nu,\, t)}{\int_0^{2\pi}\int_0^{\pi} G(\theta,\, \varphi,\, \nu)\sin\theta d\theta d\varphi} \tag{3}$$

$$T_A(\upsilon,\, t) = T_W(\nu,\, t)(1 - |\Gamma|^2). \tag{4}$$

It is expected that foregrounds are inherently smooth and can be described using "Maximally Smooth" (MS) functions, whereas, over a sufficiently wide bandwidth, the ERA signal is not smooth. This is similar to the context of the global

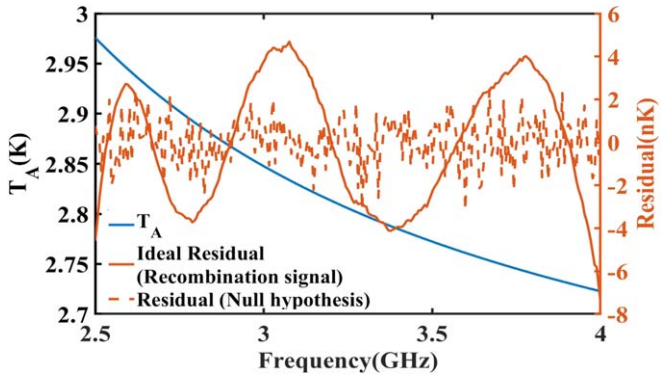

Figure 4. The mock-sky spectrum (left axis—antenna temperature) and residual on fitting the mock spectrum with an MS function ideal antenna (right axis—residual temperature) when observing the sky with an ideal antenna having radiation pattern ($\sin^2\theta$ for $\theta = 0°$–$90°$, 0 for $\theta = -90°$–$0°$) over the full frequency range. The residuals obtained by fitting the sky spectrum with and without the recombination lines, using the pipeline in Figure 3, are clearly distinguishable.

redshifted 21 cm signal from CD and EoR. This has motivated the development of mathematical formalisms to describe "smooth" foregrounds that are not fully described by a simple power law. These include MS functions (Rao et al. 2015) and "MaxSmooth" algorithms (Bevins et al. 2021). As MS functions have been in a feasibility study in the context of the ERA signal, in this work we use MS functions as the smooth function of choice.

An MS function of order n is an nth-order polynomial whose derivatives of order 2 and higher do not have any zero crossings, within the domain of interest as in the following equation:

$$\frac{d^m f(x)}{dx^m} = \sum_{i=0}^{n-m} \frac{(m+i)!}{i!} p_{m+i}(x - x_0)^i$$
for all m in the range 2, 3 ,..$(n-1)$ *and*
p_{m+i} constrained to have no zero crossings. (5)

On subtracting a sky spectrum with a best-fit MS function, the smooth components—including the foregrounds and a smooth part of the cosmological signal—are separated, leaving any spectrally complex (nonsmooth) signal behind in the residual. In an ideal case, the residual contains only the baseline-subtracted ERA signal. Beyond foreground separation, we adopt MS functions to quantify antenna performance. The rms of the residual on fitting and subtracting an MS function from the mock spectrum serves as the metric of antenna performance. The lower the rms of the residual, the better the antenna. As a demonstration, we generate a mock spectrum generated using an ideal, frequency-independent antenna with a beam described by $\sin^2\theta$ for $0 <= \theta <= 90$ and by 0 for $-90 <= \theta < 0$, over the entire bandwidth. This spectrum is then fit with an MS function. The residual on subtracting the fit from the mock spectrum is distinct between the case when the ERA signal was present and the null hypothesis case, when it is absent, as shown in Figure 4. Thus, in an ideal case, any antenna-generated spectral features can leave behind residuals with rms of $\mathcal{O}(10^{-9})$ or lower (if ERA signal is absent or fainter), when T_A is fit with an MS function, with the exact amplitude determined by the thermal noise in the spectrum. The rms of thermal noise included in the pipeline is $\mathcal{O}(10^{-9})$. This translates to antenna chromaticity to less than one part per billion. Achieving chromaticity $\lesssim$1 part in 10^9 is a daunting task. Keeping this in mind, novel techniques are being explored to be able to detect these lines using other methods of foreground and ERA signal separation, which supplement the MS function approach presented in this paper. These techniques are beyond the scope of this work.

4. Characterization of Standard Antennas for Detecting the ERA Signal

UWB antennas, such as the log periodic antenna, horn, and Vivaldi, to name a few, can cover bandwidths spanning even a decade. However, these antennas do not meet our design requirements in the 2.5–4 GHz frequency range. Two standard antennas, Vivaldi and horn, have been designed and evaluated within the pipeline, to demonstrate the same, along with a standard planar dipole. The results from the latter show the necessity to adopt electrically small antennas. The spectral chromaticity introduced by the antenna return loss shapes and beam chromaticity become increasingly apparent through the residuals obtained from the validation pipeline.

4.1. Planar Short Dipole Antenna

Before exploring standard broadband antennas, the performance of a planar short dipole antenna is investigated. This serves as a reference with respect to which improvement in the performance of conventional and custom broadband antennas can be compared. A single-polarized dipole antenna was designed and simulated in the CST Studio Suite (CST Microwave Studio 2023). The dipole was designed on a Rogers RT Duroid 5880 substrate with $\epsilon_r = 2.2$ and $h = 1.6$ mm. The dipole one arm length was optimized to be $l = 11$ mm, with a gap of 3 mm between the arms. To replicate practical observing conditions, the dipole was simulated with a metallic ground plate of size $gnd = 140$ mm over soil at a height of 20 mm. The designed dipole, along with the ground plane and soil, is shown in Figure 5(a). The soil was modeled as sandy and dry, with an $\epsilon_r = 2.55$ and $\tan\delta = 0.0062$. In the X- and Y-axes, the soil has a finite width of the order of 3 skin depths at 2 GHz, and open boundaries with vacuum space were implemented. In contrast, along the Z-axis, an open boundary was used without additional space to create an effectively infinite soil along that direction. The antenna exhibits a resonance at 3.5 GHz in its S_{11} magnitude response, as shown in Figure 6. In order to decouple the effect of return loss and the beam chromaticity, the antenna was validated in two configurations. Initially, the radiation pattern alone was considered in the pipeline, and the final T_A spectrum was fit with an MS function as described in Section 3. In practice, this is equivalent to correcting the sky spectrum for the antenna return loss in post-analysis using an in situ S_{11} measurement. The MS fit is subtracted from T_A to obtain a residual spectrum. T_A and the residual spectrum are shown in Figure 7(a). A sky spectrum at these frequencies has temperatures less than 10 K; however, the soil temperature (300 K) weighted by the back lobe results in a hotter mock spectrum. The beam chromaticity alone contributes to a residual rms of ~200 mK. Subsequently, validation was carried out for the case, including the effects of both return loss and beam pattern. The resulting T_A spectrum in Figure 7(a) clearly shows the effect of return loss shape. The residual obtained in this case has an increased rms of ~600 mK and is attributed to the inflections in return loss.

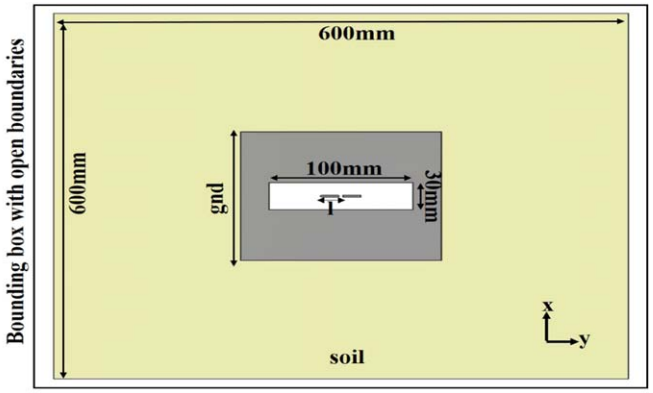

(a)

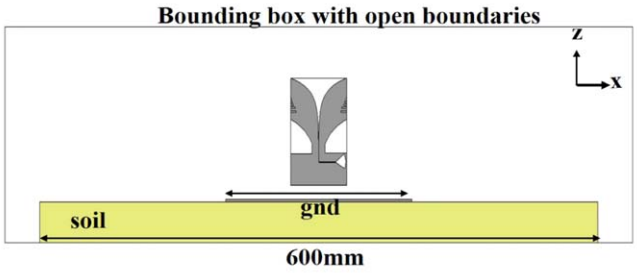

(b)

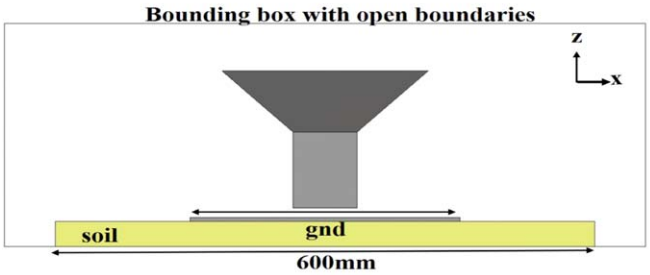

(c)

Figure 5. (a) Top view of the single-polarized planar short dipole antenna placed above ground plate on soil ($gnd = 140$ mm, $l = 11$ mm). (b) Side view of the Vivaldi placed above ground plate on soil ($gnd = 140$ mm). (c) Side view of the horn antenna placed above the ground plate of dimension $gnd = 140$ mm over soil.

4.2. Vivaldi Antenna

The typical approach to achieving broadband characteristics in Vivaldi antennas involves the excitation of multiple modes in surface currents, and these design principles are firmly established (Schaubert et al. 1985). A Vivaldi antenna was designed to operate between 2.5 and 4 GHz, by building on the reconfigurable Vivaldi antenna design detailed in Sathish et al. (2022). The antenna was designed on a Rogers RT Duroid 5880 substrate with $\epsilon_r = 2.2$ and $h = 1.6$ mm using the CST Studio Suite. Since the Vivaldi antenna operates in an end-fire configuration, it was positioned vertically, to have a beam toward zenith. As in the case of the planar dipole antenna, the Vivaldi antenna was placed over a metallic ground plate with a width of $gnd = 140$ mm over soil, at a height of 20 mm. The soil ϵ, tanδ, and boundary conditions are identical to those used in the case of the planar short dipole antenna. The designed Vivaldi, along with the ground plane and soil, is shown in Figure 5(b). The $|S_{11}|$ of the designed antenna is shown in Figure 6, and it has at least two inflection points. For the mock spectrum generated using the beam chromaticity alone, the rms of the residual is ∼300 mK, as shown in Figure 7(b). The residual obtained for the case including the effects of both return loss and beam pattern has an increased rms of ∼400 mK,

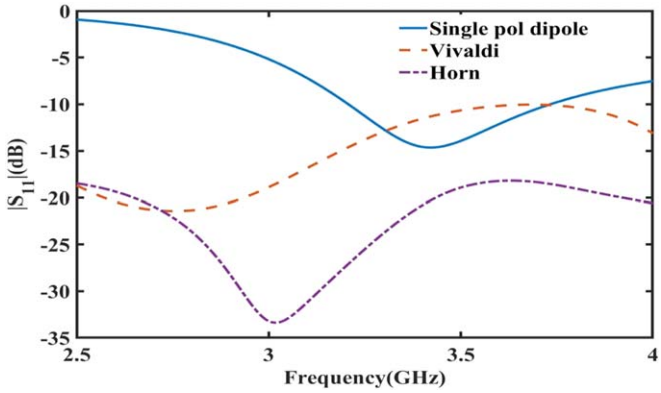

Figure 6. Simulated $|S_{11}|$ for the single-polarized planar short dipole (Figure 5(a)), Vivaldi (Figure 5(b)), and horn (Figure 5(c)) antennas.

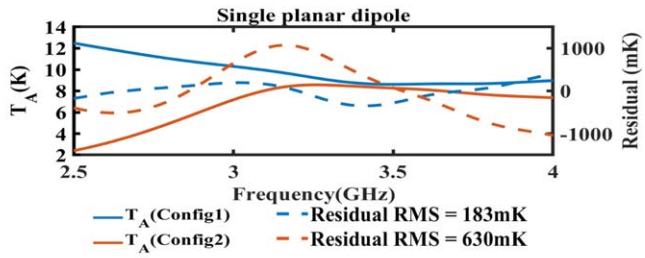

(a)

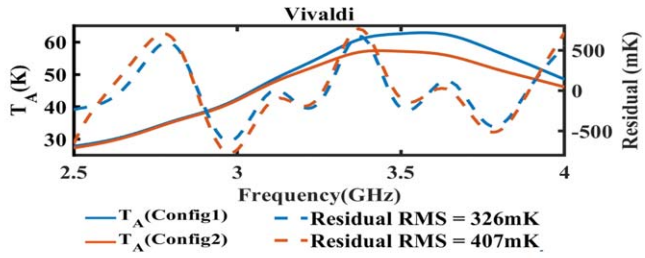

(b)

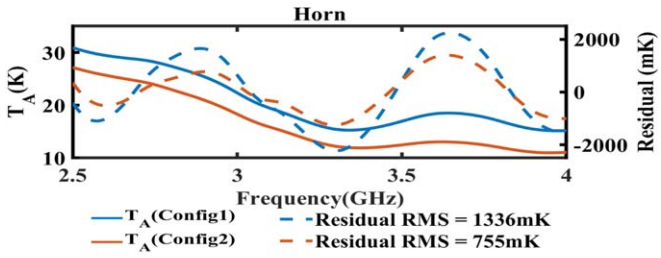

(c)

Figure 7. Mock spectra and resulting residuals after validating the standard antennas in the pipeline (Figure 3) in two configurations: Config1—using only beam; Config2—using both return loss and beam. (a) Single-polarized planar dipole antenna (Figure 5(a)) (residual rms Config1 = 183 mK, Config2 = 630 mK). (b) Vivaldi antenna (Figure 5(b)) (residual rms Config1 = 326 mK, Config2 = 407 mK). (c) Horn antenna (Figure 5(c)) (residual rms Config1 = 1336 mK, Config2 = 755 mK). Left axis: antenna temperature; right axis—residual.

as shown Figure 7(b), and is attributed to the inflections in return loss. Nonetheless, the T_A spectrum does not exhibit significant alterations, due to the near-unity transfer function value associated with the well-matched return loss. The Vivaldi performs better than the planar short dipole antenna, as the rms values of the residual in both mock spectra are lower than the corresponding cases of the planar short dipole. However, the absolute value of the rms continues to be $\mathcal{O}(100)$ mK.

4.3. Horn Antenna

A rectangular horn antenna, popularly used for UWB applications, achieves its wideband performance through multiple resonances, similar to the Vivaldi antenna. A horn was designed using the standard design principles given in Balanis (2005) and positioned 20 mm above the metallic ground plate (*gnd* width square plate) over soil. The simulation setup is identical to the one used for the Vivaldi antenna and the planar short dipole antenna. The complete model is shown in Figure 5(c), and the $|S_{11}|$ is given in Figure 6. Two mock spectra are generated for the horn antenna, in configurations similar to the dipole and Vivaldi antennas. For the case with just the pattern included, the rms of the residual obtained is $\sim$1 K, as shown in Figure 7(c). The residual rms for the case including both the return loss and pattern is $\sim$700 mK, as shown in Figure 7(c). The T_A spectrum in both configurations shows minimal variation, due to the well-matched return loss. In both cases, the residual rms values remain higher than those of the Vivaldi antenna and the planar short dipole antenna.

4.4. A Comment on Custom-designed Antennas Explored in the Literature

To make accurate measurements of the absolute sky spectrum better than existing ones over the gigahertz frequency range, we require a chromaticity better than 1 part in 1000, effectively translating to a residual $\mathcal{O}(10)$ mK in a spectrum of effective temperature $\mathcal{O}(10)$ K. We conclude that residual temperatures, as illustrated in Figure 7, indicate that the chromaticities of standard broadband antennas investigated result in an rms of $\mathcal{O}(100)$ mK and do not readily meet this requirement. Furthermore, we conclude that optimizing either the beam or return loss alone is insufficient. It is imperative to concurrently optimize both aspects in order to achieve a reduction in residual rms. A custom-designed antenna with minimal beam chromaticity and smooth return loss is recommended. Such antennas have been proposed for the detection of the EoR signal in the range of 40–200 MHz, which has similar requirements. Subrahmanyan et al. (2016) describe wideband antennas for precision cosmology experiments below 300 MHz and also present a sphere–disk monopole antenna. However, they only consider the effect of return loss in their design and do not test the effect of beam-chromaticity-induced spectral features. Similarly, Raghunathan et al. (2020) also propose a frequency-independent spherical monopole antenna with a residual of $\mathcal{O}(mK)$ in return loss but do not meet an overall smooth criterion on the full spectrum considering both the full-beam and return loss, with beam chromaticity of $\mathcal{O}(10\%)$. A related study in Raghunathan et al. (2021) presents the design and characterization of a cone–disk, antenna including a comprehensive analysis of antenna performance when the antenna is deployed over soil and over water, and highlights the impact of the operating environment on antenna behavior. In the same frequency range, there is a proposal for a broadband HIBiscus antenna in Jáuregui-García et al. (2017), intended for use in the SCI-HI experiment (Voytek et al. 2014). This antenna demonstrates a nonuniform return loss and substantial beamwidth variation of over 25° across different frequencies. While EoR signal detection experiments have a strong legacy, experiments aimed at the ERA signal are relatively recent, and there exists a limited body of existing literature. Raghunathan et al. (2015) and Kavitha et al. (2021) present antenna designs aimed at ERA signal detection for APSERa. In the former article, a monopole antenna is proposed with its beam directed at 30° from the zenith. The antenna also exhibits 10% dispersion in the beam, along with multiple ripples in measured return loss. The latter work proposes a single-polarized dipole antenna with Robert's balun. However, its return loss displays several inflection points within the passband, in addition to a 6% beam dispersion.

Section 5 presents a dual-polarized fantail-shaped dipole antenna characterized by a smooth return loss and beam chromaticity requirements better than the standard broadband antenna discussed above and better than the antenna presented in the literature in the ERA signal detection context.

5. Design of Dual-polarized Fantail-shaped Dipole Antenna

Crossed dipole antennas have been used and studied extensively for current and future wireless communication systems. Current research on crossed dipole antennas focuses primarily on improving performance parameters like gain, bandwidth, form factor, and polarization isolation, employing various optimization techniques. These involve use of metamaterial-based reflectors (Cui et al. 2017; Li et al. 2018), usage of cavity structures for gain enhancement (Saurav et al. 2015b, 2015a), introduction of multiple resonances to expand operating bandwidth (Saurav et al. 2016; Wen et al. 2018), and inclusion of magnetoelectric dipole structures to enhance pattern stability (Ye et al. 2020; Shang et al. 2023). Crossed dipoles are extensively used in wireless base stations, satellite communication (Ta & Park 2017; Park 2014), and more recently wireless power transfer research (Liao et al. 2022). Ta et al. (2015) provide a detailed review of diverse designs and alternative applications of crossed dipoles. Despite the broad spectrum of applications and innovations in these antennas, their direct applicability to cosmology experiments is limited, due to the constraints detailed in the preceding sections. In response to these constraints, the proposed fantail antenna design is purpose built exclusively for precision cosmology experiments. While the fundamental design principles for crossed dipole antennas are well established, the novelty lies in the customization of this structure to align with the stringent requirements mentioned in Section 2.

The antennas that were designed and evaluated in Section 4 do not meet the criteria outlined in Section 2, resulting in residuals with rms $\mathcal{O}(100)$ mK in the validation pipeline. These standard antennas achieve wide bandwidths by having multiple resonances within the band, leading to high-order modes in the surface current distribution, thereby altering the radiation pattern across frequency. In the fantail antenna presented here, minimal chromaticity in the beam is achieved by making the antenna electrically small. However, as demonstrated by the single planar dipole antenna evaluated in Section 4, we note that merely having an electrically small antenna is insufficient. Acceptable performance necessitates an electrically small

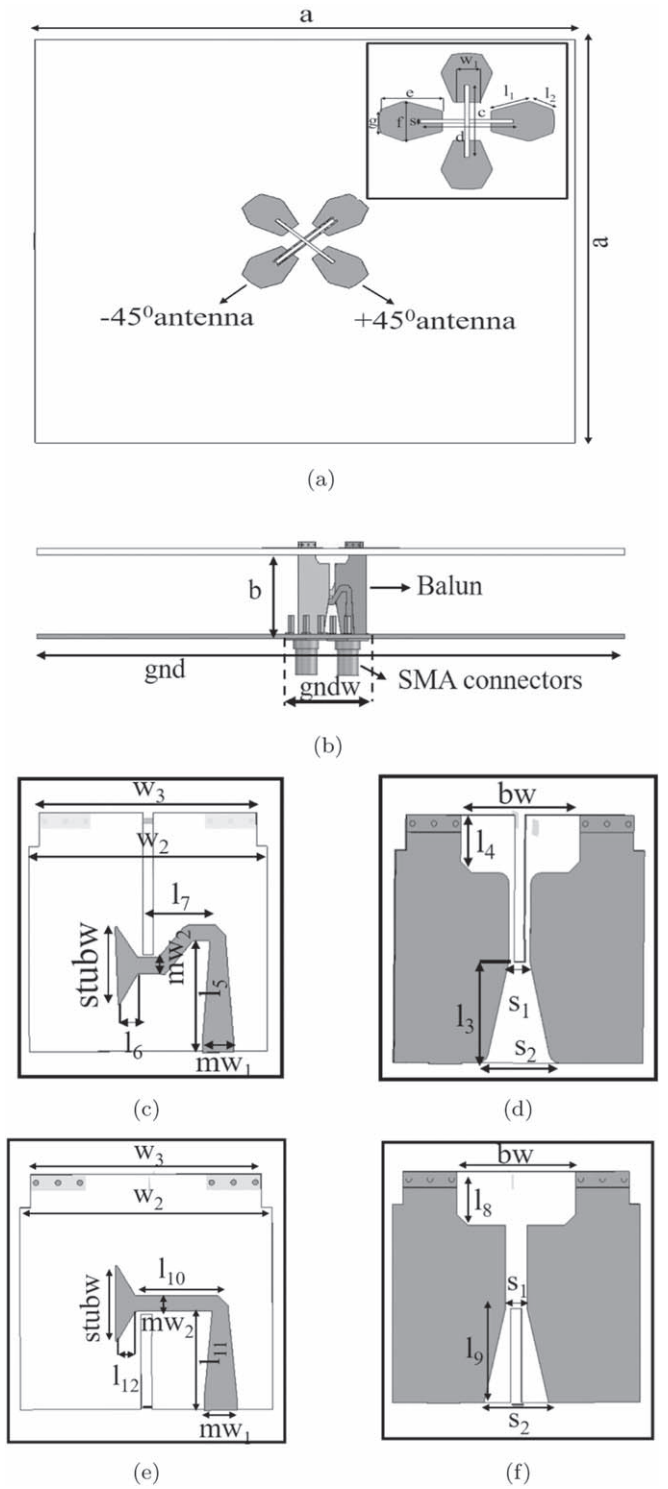

Figure 8. (a) Top view of the dual-polarized fantail dipole antenna on substrate (inset—zoomed-in version of the dipole with dimensions). (b) Side view of the antenna with ground plane. (c) Balun of the +45° polarized antenna (top view). (d) Balun of the +45° polarized antenna (bottom view). (e) Balun of the −45° polarized antenna (top view). (f) Balun of the −45° polarized antenna (bottom view). All the dimensions are given in Table 1.

antenna with $|S_{11}|$ better than 3 dB and a smooth shape, with smoothness as outlined in Section 3. The presence of metallic ground beneath an antenna will introduce ripples in its main lobe and in its return loss. Conversely, without the ground plane, the temperature seen by the antenna's back lobe can

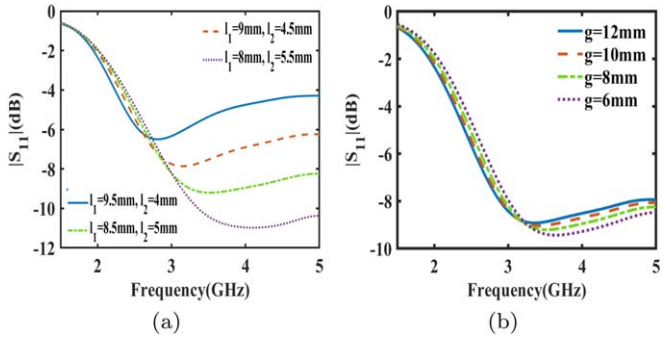

Figure 9. (a) Magnitude of S_{11} simulated by parametric sweep of l_1, l_2 with $g = 7$ mm, $w_1 = 7$ mm, $e = 15$ mm, $f = 10$ mm. (b) Magnitude of S_{11} simulated by parametric sweep of g with $l_1 = 8.5$ mm, $l_2 = 5$ mm, $e = 15$ mm, $f = 10$ mm.

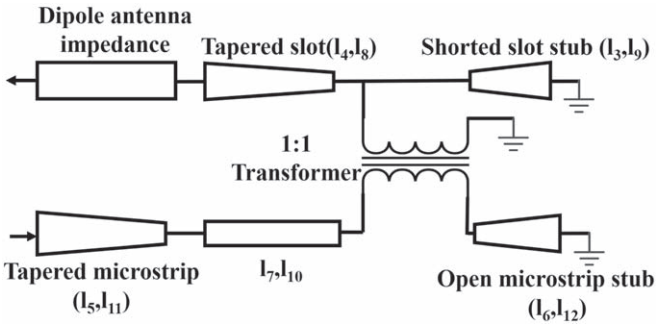

Figure 10. Equivalent circuit of the balun, with dimensions given in Table 1.

dominate sky temperature, thereby leading to an increase in the system temperature. Keeping these considerations in mind, a dual-polarized dipole antenna has been carefully designed, with smooth return loss and broad resonance centered at 3.5 GHz, having a frequency-independent beam in the 2.5–4 GHz band. The antenna assembly comprises an upper substrate containing the dual-polarized antenna, featuring an X-shaped slot in the center to accommodate two balun substrates beneath, which are oriented perpendicular to the antenna in a puzzle-like arrangement. Additionally, there is a finite ground plane measuring 140×140 mm^2 positioned at a 20 mm separation from the antenna, as illustrated in Figures 8(a) and (b).

The design process for the proposed dual-polarized fantail antenna commenced with developing a single-polarized dipole without a balun. The goal was to achieve resonance at 3.5 GHz, with a monotonically decreasing return loss from 2.5 to 3.5 GHz. This was achieved by varying the width and length of the arm, thereby fixing the parameters e and f. The antenna's return loss was further optimized to be smooth by shaping the dipole arms into a fantail configuration akin to a hexagonal shape. This process utilized a combination of the standard parametric sweeps in CST software and manual tuning of the three variables l_1, l_2, g, which were constrained by fixed design parameters e, f. Figure 9(a) illustrates the variation in the $|S_{11}|$ while sweeping the parameters l_1 and l_2, with the other variables held constant at $g = 7$ mm, $w_1 = 7$ mm, $e = 15$ mm, and $f = 10$ mm. As the overall length of the arm is fixed at e, the lengths l_1 and l_2 are swept simultaneously. Analysis of the parametric curves indicates that $|S_{11}|$ improves as l_1 decreases and l_2 increases. Therefore, the lengths were optimized at $l_1 = 8$ mm and $l_2 = 5.5$ mm. Figure 9(b) demonstrates the effect of sweeping g, with the other variables at $l_1 = 8$ mm,

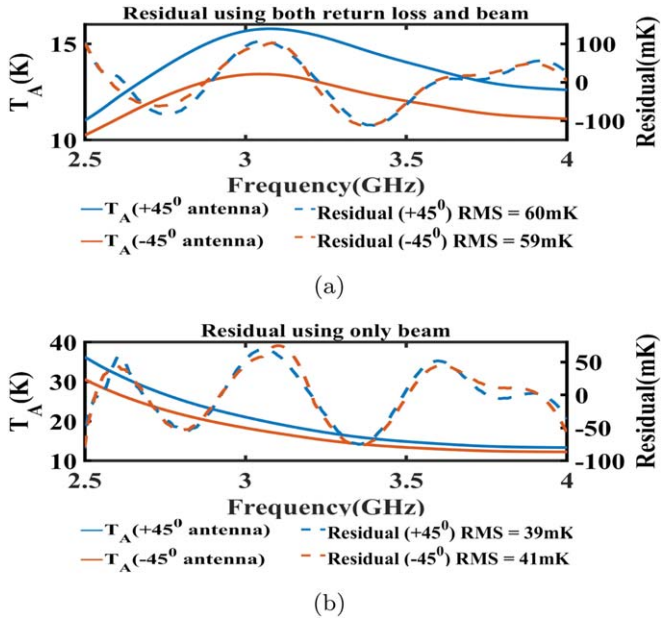

Figure 11. Mock spectra and resulting residuals after validating the fantail antenna over soil in two configurations. (a) Taking both return loss and beam into consideration (+45° antenna residual rms = 60 mK, −45° antenna residual rms = 59 mK). (b) Taking only beam into consideration (+45° antenna residual rms = 39 mK, −45° antenna residual rms = 40 mK). Left axis —antenna temperature; right axis—residual.

Table 1
Dimensions of the Antenna and Balun

Parameter	Value	Parameter	Value	Parameter	Value
a	140	b	20	c, d	21
gnd	140	e	15	f	10
g	7	s	1.1	$gndw$	25
w_1	4.6	w_{22}	8.5	w_3	20
l_1	8.5	l_2	5	l_3	10
l_4	5.2	l_5	10.2	l_6	3.3
l_7	7.1	l_8	7.1	l_9	10.5
l_{10}	7.5	l_{11}	9.2	l_{12}	3
s_1	2	s_2	3	$stubw$	7
mw_1	3	mw_2	1.5	bw	7

Note. All dimensions are in units of mm.

$l_2 = 5.5$ mm, $e = 15$ mm, and $f = 10$ mm. This tuning led to setting $g = 6$ mm for better-matched $|S_{11}|$. After this, the design was extended to two orthogonal linear polarizations in a dual-polarization configuration. Subsequently, a microstrip-based feeding method was chosen for the dipole, primarily to reduce insertion loss and provide flexibility in shaping the balun, thereby improving impedance matching. To feed the dual-polarized antennas, two baluns were designed to fit together seamlessly, similar to a jigsaw puzzle, as shown in Figure 8(b). The balun developed for the fantail antenna proposed in this study utilizes an integrated microstrip-to-slotline transition-based balun, derived from the integrated balun circuits proposed in Ye et al. (2021) and Liao et al. (2022).

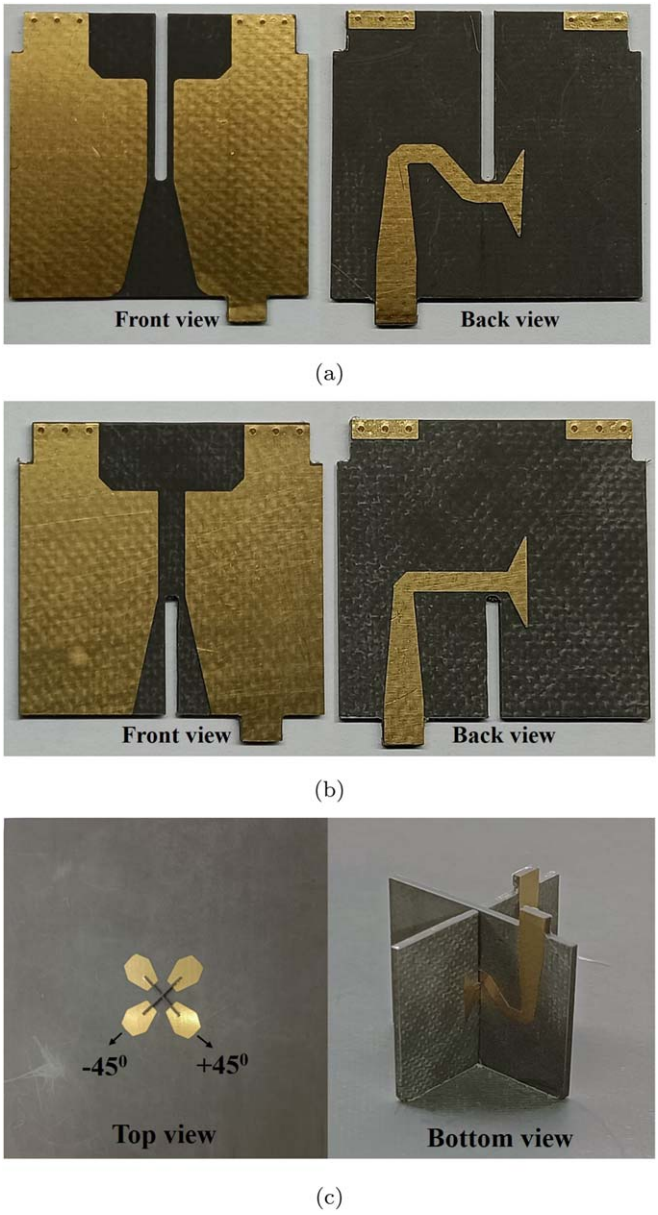

Figure 12. (a) Front view and back view of the fabricated balun for +45° polarized antenna. (b) Front view and back view of the fabricated baluns for −45° polarized antenna. (c) Top view and bottom view of the fabricated dual-polarized fantail antenna fitted with the baluns.

Figure 10 displays the balun's equivalent circuit, with the lengths of various lines detailed in Table 1. Resonance at 3.5 GHz was achieved by tuning the microstrip stubs (l_6 and l_{12}) and slotline stubs (l_3 and l_9), with modifications made to their shapes to ensure a smooth return loss. The tapered slotline impedance (l_4 and l_8) was optimized to match the input impedance of the dipole antenna, while the input tapered microstrip lines (l_5 and l_{11}) were adjusted to match the input impedance of the SMA connector. Lastly, the lengths of transmission lines l_7 and l_{10} were adjusted to attain identical resonances for both antennas. Subsequently, the antenna was subjected to a final optimization, which involved the incorporation of the balun and input SMA connectors. The design was simulated in the CST design studio software. The final optimized dimensions for both the antennas and the balun are given in Table 1, and these dimensions are indicated in Figure 8 for reference.

(a) (b)

Figure 13. (a) Setup for the measurement of the return loss of the dual-polarized fantail antenna on soil. (b) Pattern measurement setup in an anechoic chamber.

To facilitate a consistent comparison with the standard broadband antennas described in Section 4, the fantail antenna was simulated with soil underneath it, and the results were subsequently validated. The simulation settings of the standard antennas were replicated, and the residuals were estimated in two different configurations in the pipeline: (i) taking only the beam into consideration, and (ii) taking both return loss and beam into consideration. The residual obtained at the output of the validation pipeline in both cases is shown in Figure 11. From Figure 11(a) we note that the residual rms when both return loss and radiation pattern are considered is ∼60 mK for both polarizations, indicating identical performance between the two antennas. The residual rms further reduces to ∼40 mK, when only the beam is considered, as shown in Figure 11(b). The residual rms of the fantail antenna is nearly 10 times lower than that of the previously described standard antennas. Additionally, the antenna temperature is comparatively lower than the standard horn and Vivaldi antennas, indicating a reduced presence of back lobes in the fantail antenna. These attributes render the proposed fantail antenna particularly well suited for cosmological applications, including making an absolute measurement of the radio sky at gigahertz frequencies, thereby improving on existing measurements to resolve the debate on the existence of an excess radio background. Thus, the designed antenna was fabricated, and its properties were measured for comparison with the simulations.

6. Fabrication, Analysis, and Measurement

The fantail antenna designed and detailed in Section 5 was fabricated on a Rogers RT Duroid 5880 substrate with $\varepsilon = 2.2$ and height $h = 1.6$ mm, and the baluns were fabricated on an RT Duroid 5880 substrate with height $h = 1$ mm. The top antenna substrate has an X-shaped slot at its center, through which the balun substrates were inserted. Electrical connections between the balun and the dipole arms were established through soldering after inserting each balun into its slot, ensuring a robust connection. Subsequently, the balun cards were firmly attached to a compact ground plate featuring grooves. SMA connectors were then fixed onto this ground plate and soldered to the baluns. Foam support structures ($\epsilon_r \sim 1$) were used to secure the antenna substrate in place and

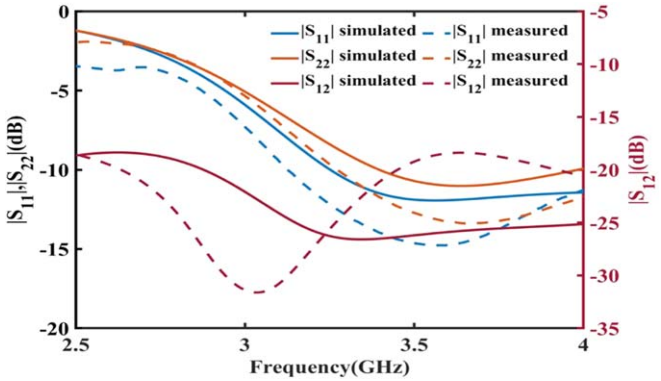

Figure 14. Simulated and measured magnitude of *S*-parameters of the fantail antenna. Left axis—$|S_{11}|$ and $|S_{22}|$; right axis—$|S_{12}|$.

provide some ruggedness to the entire assembly. Lastly, the small ground plane was affixed to a larger, finite ground plate of 140×140 mm^2 size. This assembly also offers the flexibility to attach the antenna to ground planes of various sizes as needed. The spacing between the antenna and the ground plane is determined by the height of the balun cards, and this distance remains fixed and cannot be adjusted. Figure 12 shows the fabricated antenna along with the baluns. For efficient cable connection, two right-angle SMA adapters were connected to the affixed SMA connectors. The antenna *S*-parameters were then measured in the field over the soil using a Keysight Fieldfox N9916B analyzer. Two equal-length cables were used, one each per polarization. The calibration was carried out at the end of the RF cables along with the right-angle connectors to calibrate the cable response from the return loss. Figure 13(a) shows the measurement setup for antenna return loss measurement on the soil. Antenna pattern measurements were conducted in an anechoic chamber, as shown in Figure 13(b). Additionally, return loss measurements were performed within the same setup. Figure 14 shows the *S*-parameter results, both simulated and measured, for the anechoic chamber configuration where no soil is present beneath the antenna. It can be observed from Figure 14 that the measured return loss for both antennas exhibits a smoothly varying function. However, the measured return losses exhibit an overall reduction of ∼1–2 dB, which can be attributed to the copper tapes used for securing the connections between the ground plane and balun. The shift in the resonance dips in the measured results is attributed to the fabrication tolerances in the antenna. However, the shift does not significantly hinder us as long as the return loss exhibits smoothness. The isolation between the two polarizations is greater than 20 dB in both simulations and measurements. The radiation pattern was measured in the anechoic chamber at 101 frequency points in both E-plane and H-plane cuts, considering both Co-pol and Cross-pol for both polarizations. The measured pattern exhibits 40° beamwidth in the E-plane and 80° beamwidth in the H-plane, with Cross-pol radiation levels greater than 15 dB. The Co-pol patterns were observed to have close agreement between the simulated and measured values across all frequencies, with a maximum rms error of 0.06. For brevity, the simulated and measured patterns are plotted only at 3 GHz for both antennas in Figure 15. The pattern variation in both E-plane and H-plane across frequencies for both arms of the dipole are depicted in Figure 16. The peak gain variation and half-power beamwidth variation across frequency for measured patterns are plotted in Figures 17 and

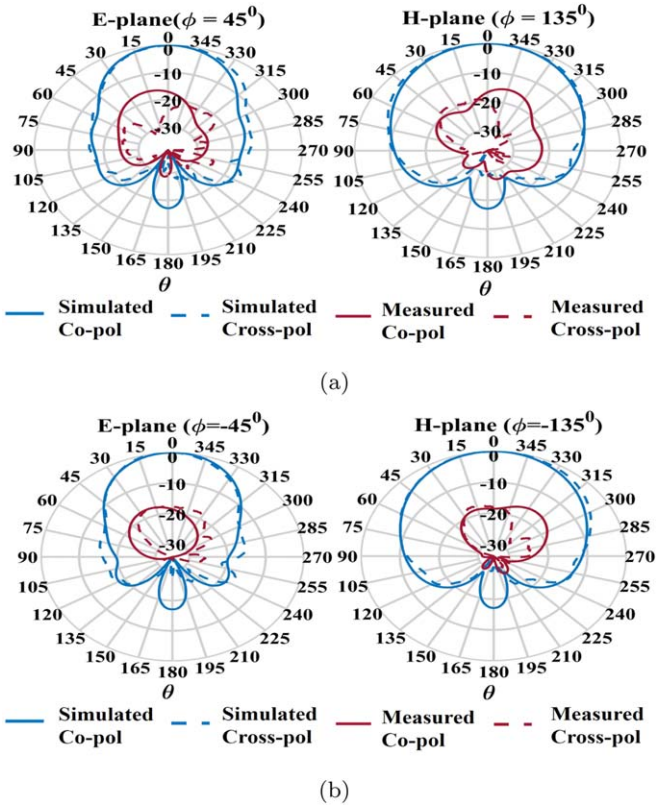

Figure 15. (a) Simulated and measured Co-pol and Cross-pol radiation pattern (E-plane and H-plane) at 3 GHz for +45° polarized antenna (Figure 12(c)). (b) Simulated and measured Co-pol and Cross-pol radiation pattern (E-plane and H-plane) at 3 GHz for −45° polarized antenna (Figure 12(c)).

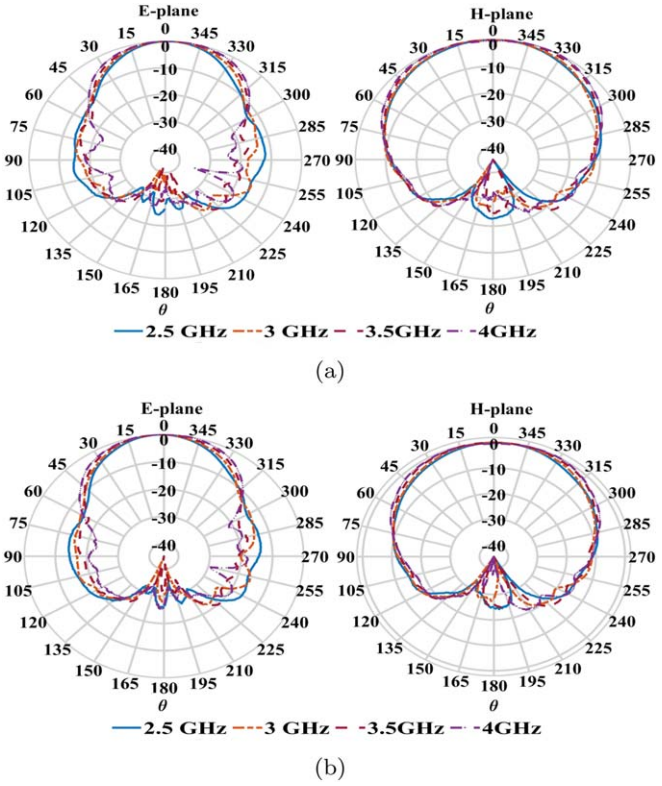

Figure 16. (a) Measured E-plane and H-plane radiation pattern across the 2.5–4 GHz band for +45° polarized antenna (Figure 12(c)). (b) Measured E-plane and H-plane radiation pattern across the 2.5–4 GHz band for −45° polarized antenna (Figure 12(c)).

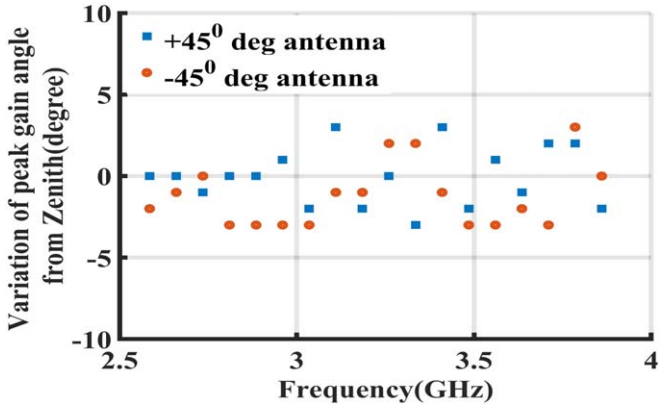

Figure 17. Variation of peak gain angle from zenith for both the polarizations (Figure 12(c)). The maximum variation in both polarizations is ±3° from zenith.

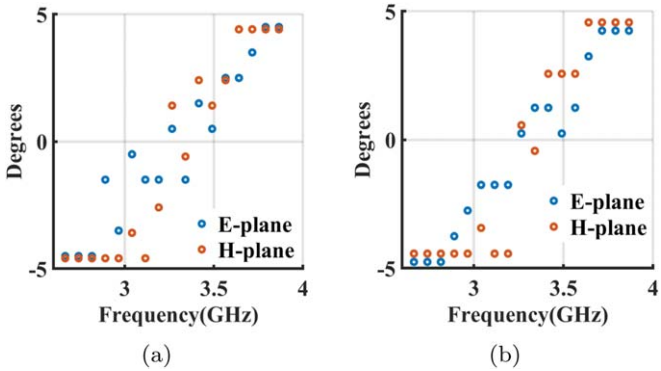

Figure 18. (a) Measured E-plane and H-plane radiation pattern half-power beamwidth variation across the 2.5–4 GHz band for +45° polarized antenna. (b) Measured E-plane and H-plane radiation pattern half-power beamwidth variation across the 2.5–4 GHz band for −45° polarized antenna. *Y*-axis shows the variation of the beamwidth from the center frequency (3.25 GHz) beamwidth.

18, which show that both antennas exhibit a peak gain angle variation of ±3° from zenith and a beamwidth variation of ±5° from the center frequency beamwidth. This corresponds to a variation of only 0.83% for peak gain and 1.5% for beamwidth, highlighting their stability across frequency. These characteristics outperform existing antennas in the literature for the ERA experiments. Table 2 presents a comparative analysis, demonstrating the superior performance of the proposed fantail antenna compared to antennas custom designed for global cosmological signal detection experiments found in the literature. Despite differences in the dynamic range and operating frequency between EoR and ERA signal detection experiments, the antenna design requirements adopted by the experiments referenced in the table are similar. The comparison is intended for the reader familiar with antenna design for global EoR signal detection experiments to provide a context for requirements for ERA signal detection. The table aims to illustrate the similarity in antenna design approaches and compare the relative beam dispersion and S_{11} characteristics of these antennas, and the absolute values of numbers in the table across EoR and ERA experiments are not to be compared.

The antenna measurements from the anechoic were subsequently passed through the validation pipeline, replacing the fixed temperature of 300 K for the lower hemisphere with the

Table 2
Comparison Study of Fantail Antenna in Different Configurations with Other Custom Antennas in the Literature

S.no	Reference	Frequency Band	Antenna	Return Loss Characteristics	Beam Characteristics	Validation Pipeline	Residue level
1	(Raghunathan et al. 2020)	50–200 MHz	Spherical monopole	0.05 dB (50 MHz) to 10 dB (200 MHz) smoothly varying	Measured pattern with 10%–12% dispersion in 3 dB beamwidths	Only return loss	order of 10^{-4} K
2	(Mahesh et al. 2021)	50–100 MHz	Dipole antenna on finite ground plane	9 dB (50 MHz) to 12 dB (90 MHz) non-smoothly varying	Beam pointed at zenith with maximum gain dispersion of 0.2	Measured return loss and simulated beam patterns	Residues of the order of 200 mK
3	(Cumner et al. 2022)	50–135 MHz	Blade dipole	Well-matched return loss but with inflections	Beam toward zenith and optimized to have minimal chromaticity	Measured return loss and simulated beam patterns	Residues of the order of 155 mK
4	(Raghunathan et al. 2015)	2–4 GHz	Discone monopole	Well-matched return loss with ripples	Beam pointed at 30° from zenith, with 10% beam dispersion and 30% peak gain variation	Only return loss	Not validated
5	(Kavitha et al. 2021)	2–4 GHz	Shaped dipole	5 dB flat return loss in 2.5–3.5 GHz	Zenith-pointed beam with 6% dispersion in 3 dB Beamwidth	Only return loss	order of 10^{-3} K (from 2.5–3.3 GHz)
6	**This work**	**2.5–4 GHz**	**Fantail-shaped dipole with finite ground plane (no soil)**	**Smooth return loss with one inflection at 3.5 GHz**	**Zenith-pointed beam with 1.5% 3 dB beamwidth dispersion**	**• Using both return loss and Beam** **• Using only beam**	**• (Sim.) $\sim$ 2.2 mK, (Meas.) $\sim$ 31mK** **• (Sim.)0.06mK, (Meas.)0.7mK**
7	**This work**	**2.5–4 GHz**	**Fantail-shaped dipole with finite ground plane and soil**	**Smooth return loss with one inflection at 3.5 GHz**	**Zenith-pointed beam with 3% 3 dB beam-width dispersion**	**• Using both return loss and Beam** **• Using only beam**	**• RMS $\sim$ 60mK** **• RMS $\sim$ 40mK**

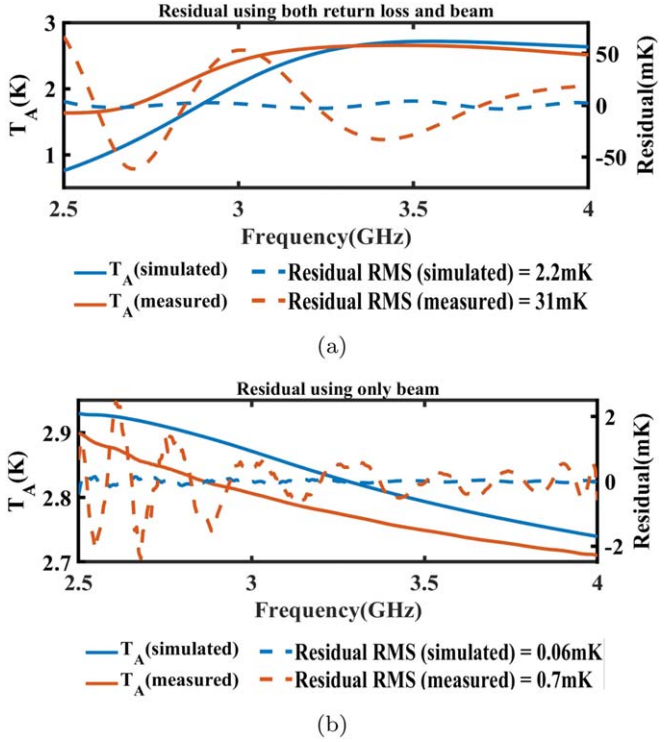

Figure 19. Mock spectra and resulting residuals after validating the fantail antenna (+45° polarization) over a finite ground plane without soil in two configurations. (a) Taking both return loss and beam into consideration (residual rms (simulated) = 2.2 mK, (measured) = 31 mK). (b) Taking only beam into consideration (residual rms (simulated) = 0.06 mK, (measured) = 0.7 mK). Left axis—antenna temperature; right axis—residual.

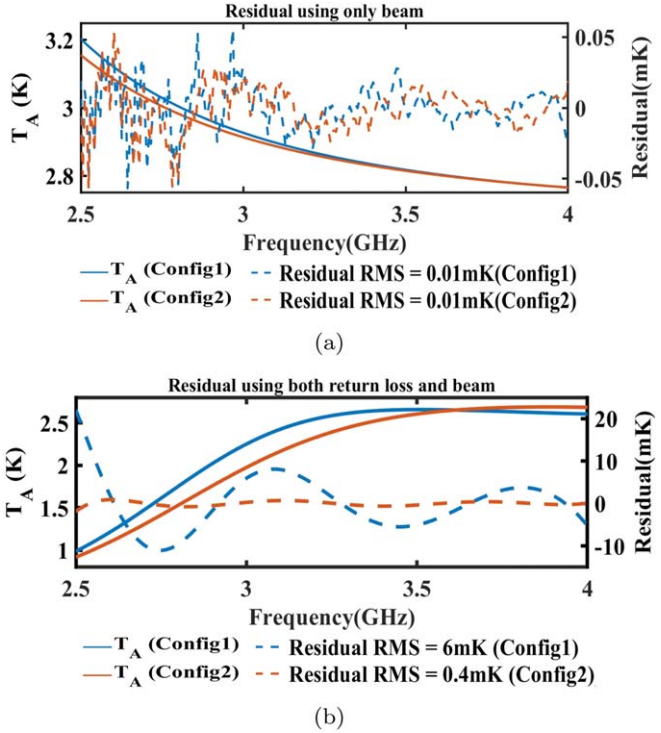

Figure 20. Mock spectra and resulting residuals after validating the fantail antenna (+45° polarization) over an infinite ground plane in two configurations: Config1—antenna with infinite ground plane and return loss resonance at 3.5 GHz; Config2—antenna with infinite ground plane and return loss resonance pushed to 3.9 GHz. (a) Taking both return loss and beam into consideration (residual rms (simulated) Config1 = 6 mK, Config2 = 0.4 mK). (b) Taking only beam into consideration (residual rms (simulated) Config1 = 0.01 mK, Config2 = 0.01 mK). Left axis—antenna temperature; right axis—residual.

sky temperature from the radio-sky model, to simulate an observation in free space. The pattern measurements in the anechoic chamber were limited to two principal cuts. However, the validation pipeline necessitates using the entire 3D pattern. To bridge this gap, the measured pattern was interpolated for the validation, resulting in a residual as shown in Figure 19 (only one polarization datum is shown, as both antennas have identical performance). For the case when only the antenna beam is considered, the rms of the residual from the measured pattern is 0.7 mK, with the value dropping to 0.06 mK for the simulations. The residual rms calculated using both return loss and beam is 2 mK for the simulations, as opposed to 31 mK for the measured results. The increase in residual while using measured results can be attributed to the interpolation error in measured patterns. Pattern measurement on multiple plane cuts will be carried out in the future to reduce this error. To explore avenues for further performance enhancement and also to assess the impact of the finite ground plane, simulations of the fantail antenna were carried out on an infinite ground plane. The utilization of an infinite ground plane effectively suppresses back lobes, resulting in the T_A shown in Figure 20(a) closely approximating the sky temperature at these frequencies. When considering only the beam, the residue rms is $\mathcal{O}(10^{-5})$ K, comparable to the case of the antenna with a finite ground plane in free space. However, when both return loss and beam are considered, the rms increases in both the infinite ground plane over soil and finite ground plane in free-space configurations. This increase can be attributed to the presence of a return loss inflection point within the band. To validate this hypothesis, a fantail antenna was designed over an infinite ground plane over soil and with a resonance toward the edge of the band, centered around 3.9 GHz. The residual obtained from the validation of this antenna is presented in Figure 20(b), where the rms, when considering both return loss and beam validation, has decreased to 0.4 mK, while the rms of the residual when only considering the beam remains unchanged. This reaffirms the takeaway message that there are two avenues to improve the antenna's performance. The first is to shift the resonance closer to the band's edge and in the extreme case all the way outside the band. The second involves refining the ground plane design to reduce back lobes. Given the reduction in residual across all cases when validating the beam alone, another aspect worth considering is the precise measurement of return loss in situ, to better than 1 part in 10^5, and subsequently removing it from the T_A spectrum.

7. Conclusions and Future Work

We have presented the antenna design requirements for a ground-based experiment seeking to detect the faint additive spectral distortions to the CMB from the ERA, drawing parallels to the requirements for redshifted global 21 cm detection experiments seeking to study CD and EoR. Using spectral smoothness as a basis for foregrounds separation, we have presented an antenna validation pipeline. Our design emphasizes the achromatic behavior of the antenna over the full band of 2.5–4 GHz. We demonstrate the order-of-magnitude improvement in the performance of a custom antenna designed in keeping with the prescribed design guidelines, compared to

conventional wideband antennas, including an electrically small ideal planar dipole antenna, Vivaldi antenna, and horn antenna. All antennas were designed with identical boundary conditions and above a metallic ground plane over soil to mimic practical conditions. These antennas were subjected to validation through a custom pipeline with an input model of the radio sky over the horizon and soil with temperature 300 K below the horizon. Mock observations were generated in two distinct configurations: one considering only the antenna beam, and the other including both return loss and beam. In both configurations, the rms values of the residual exceeded 200 mK. The fantail antenna simulated on soil using the same setup as standard antennas yielded residual ∼60 mK with both beam and pattern included in generating a mock spectrum and ∼40 mK considering beam pattern alone. This is an order-of-magnitude improvement in antenna performance compared to standard antennas. The antenna was fabricated and measured to possess a smooth return loss and an achromatic beam pattern spanning 2.5–4 GHz. The return loss is greater than 3 dB throughout the band, with resonance at 3.5 GHz and isolation between the two polarizations greater than 20 dB. The measured radiation pattern has 40° beamwidth in E-plane and 80° beamwidth in H-plane. The half-power beamwidth and peak gain of the measured radiation pattern exhibit a variation of 1.5% and 0.83% across the band, respectively. This performance was found to surpass that of existing antennas documented in the literature for the APSERa experiment. The measured antenna pattern was validated through the pipeline yielding a residual with rms ∼30 mK when considering both beam and return loss. The residuals reduced to less than 1 mK with only beam considered in the pipeline. This was followed by an evaluation of the antenna's performance with the introduction of an infinite ground plane to gain insight into the predominant contributors to the residual. This analysis resulted in a reduced residual rms of 6 mK, with the beam alone contributing a mere 0.01 mK rms temperature. An additional simulation was carried out with the same configuration as the former one, involving the modification of the antenna's return loss to position the resonance closer to the band edge, which resulted in reducing the rms further to 0.4 mK. Thus, optimizing the return loss of the fantail antenna to have resonance outside the operating band holds the potential for achieving reduced residual. Additionally, increasing the front-to-back ratio of pattern will also improve the residual.

Our forthcoming efforts will be dedicated to enhancing the performance of the designed fantail antenna through further optimization of the return loss and modifications of the ground plane design to minimize the back lobes. In addition to design considerations, efforts will also be focused on antenna modeling. Achieving an accurate measurement of the antenna's response is crucial, as it facilitates its removal from the received spectrum, thereby enhancing signal detection statistics. Therefore, efforts will be directed toward radiation pattern measurements in practical conditions and precise return loss measurements.

While improvements in antenna frequency-independent behavior will be undertaken to meet the stretch goal of achieving a chromaticity of one part per billion, there are several relevant applications for our fantail antenna with varying degrees of acceptable chromaticity or residual levels. The proposed fantail antenna having residual of the order of 10^{-3} K, along with cryogenic receiver having calibration sensitivity of 1 part in 10^4, can be used for accurate measurement of the absolute sky temperature over the full band of 2.5–4 GHz. This application holds the potential to effectively address the excess radio background problem, as substantiated by findings from the ARCADE-2 balloon experiment (Fixsen et al. 2011). In addition to the absolute sky measurements, the single element antenna, albeit with poor localization features, can be used for a blind survey of the fast radio bursts in the 2–4 GHz band. However, the localization can be enhanced by having an array of antennas with an appropriate back-end receiver used in the beam-forming mode. An improved fantail antenna with even better achromatic properties (effective chromaticity $\lesssim$1 part in 10^5) can be used to detect other spectral distortions of the CMB, such as the μ-type distortion (Sunyaev & Zeldovich 1970) or the exotic process of energy injection in the CMB, which results in spectral distortions of the CMB in the low-to-mid-gigahertz frequency range today.

Acknowledgments

K.S. thanks Mr. Debaprasad Barad for his invaluable support in the fabrication of the antennas. Additionally, K.S. and M.S. R. thank Dr. Saurabh Singh for his valuable suggestions and acknowledge the valuable support and cooperation provided by the staff at RRI and Gauribidanur Observatory for their assistance in facilitating the setup for measurements. All the authors would also like to thank Dr. K. J. Vinoy for providing the anechoic chamber facility for the pattern measurements.

ORCID iDs

Keerthipriya Sathish https://orcid.org/0000-0002-0290-0825
Mayuri Sathyanarayana Rao https://orcid.org/0000-0002-9761-3676
Debdeep Sarkar https://orcid.org/0000-0001-7993-6482

References

Balanis, C. A. 2005, Antenna Theory: Analysis and Design (New York: Wiley) Balanis
Bennett, C. L., Larson, D., Weiland, J. L., et al. 2013, ApJS, 208, 20
Bevins, H., Handley, W., Fialkov, A., et al. 2021, MNRAS, 502, 4405
Bowman, J. D., Morales, M. F., & Hewitt, J. N. 2009, ApJ, 695, 183
Bowman, J. D., Rogers, A. E., Monsalve, R. A., Mozdzen, T. J., & Mahesh, N. 2018, Natur, 555, 67
Chluba, J., Abitbol, M. H, Aghanim, Y, et al. 2021, ExA, 51, 1515
Chluba, J., & Sunyaev, R. 2006, A&A, 458, L29
Chluba, J., & Sunyaev, R. A. 2007, A&A, 475, 109
Condon, J., Cotton, W., Fomalont, E., et al. 2012, ApJ, 758, 23
Chluba, Jens, & Ali–Haimoud, Yacine 2016, MNRAS, 456, 3494
CST Microwave Studio 2023, CST MICROWAVE STUDIO, https://www.3ds.com/products/simulia/cst-studio-suite
Cui, Y., Gao, X., Fu, H., Chu, Q.-X., & Li, R. 2017, IAPM, 59, 77
Cumner, J., De Lera Acedo, E, De Villiers, D. I. L, et al. 2022, JAI, 11, 2250001
de Oliveira-Costa, A., Tegmark, M., Gaensler, B., et al. 2008, MNRAS, 388, 247
Desjacques, V., Chluba, J., Silk, J., de Bernardis, F., & Doré, O. 2015, MNRAS, 451, 4460
Fang, K., & Linden, T. 2015, PhRvD, 91, 083501
Fixsen, D. 2009, ApJ, 707, 916
Fixsen, D., Kogut, A, Levin, S, et al. 2011, ApJ, 734, 5
Fornengo, N., Lineros, R., Regis, M., & Taoso, M. 2011, PhRvL, 107, 271302
Gervasi, M., Zannoni, M., Tartari, A., Boella, G., & Sironi, G. 2008, ApJ, 688, 24
Gorski, K. M., Hivon, E, Banday, B. J, et al. 2005, ApJ, 622, 759
Hart, L., Rotti, A., & Chluba, J. 2020, MNRAS, 497, 4535
Haslam, C., Salter, C., Stoffel, H., & Wilson, W. 1982, A&AS, 47, 1

Hooper, D., Belikov, A. V., Jeltema, T. E., et al. 2012, PhRvD, 86, 103003
Jáuregui-García, J. M., Peterson, J. B., Castillo-Domínguez, E., & Voytek, T. C. 2017, 2017 IEEE Int. Symp. on Antennas and Propagation and USNC/URSI National Radio Science Meeting (New York: IEEE), 697
Kavitha, K., Raghunathan, A, Somashekar, R, et al. 2021, 2021 IEEE Indian Conf. on Antennas and Propagation (InCAP) (New York: IEEE), 367
Kogut, A., Fixsen, D. J, Chuss, D. T, et al. 2011, JCAP, 2011, 025
Kogut, A., Chluba, J., Fixsen, D. J, et al. 2016, Proc. SPIE, 9904, 99040W
Kogut, A., Abitbol, M. H, Chluba, Jean, et al. 2019, arXiv:1907.13195
Li, M., Li, Q. L., Wang, B., Zhou, C. F., & Cheung, S. W. 2018, ITAP, 66, 2610
Liao, L., Li, Z., Tang, Y., & Chen, X. 2022, Electronics, 5, 778
Maffei, B., Abitbol, M. H., Aghanim, N., et al. 2023, The Sixteenth Marcel Grossmann Meeting on Recent Developments in Theoretical and Experimental General Relativity, Astrophysics and Relativistic Field Theories: Proc. MG16 Meeting on General Relativity, ed. R. Ruffini & G. Vereshchagin, (Singapore: World Scientific), 1633
Mahesh, N., Bowman, J. D, Mozdzen, Thomas J, et al. 2021, AJ, 162, 38
Mather, J. C., Fixsen, D. J., Shafer, R. A., Mosier, C., & Wilkinson, D. T. 1999, ApJ, 512, 511
Morales, M. F., Hazelton, B., Sullivan, I., & Beardsley, A. 2012, ApJ, 752, 137
Nhan, B. D., Bradley, R. F., & Burns, J. O. 2017, ApJ, 836, 90
Park, I. 2014, JEES, 14, 299
Pattison, J. H. N., Anstey, D. J., & deLeraAcedo, E. 2023, MNRAS, 527, 2413
Raghunathan, A., Girish, B. S, Somashekar, R, et al. 2020, 2020 International Applied Computational Electromagnetics Society Symposium (ACES) (New York: IEEE), 1
Raghunathan, A., Subrahmanyan, Ravi, Uday Shankar, J, et al. 2021, ITAP, 69, 6209
Raghunathan, A., Shankar, N. U., Rao, M. S., & Subrahmanyan, R. 2015, in 2015 IEEE-APS Topical Conference on Antennas and Propagation in Wireless Communications (APWC) (New York: IEEE), 949
Rao, M. S., Subrahmanyan, R., Shankar, N. U., & Chluba, J. 2015, ApJ, 810, 3
Rao, M. S., Subrahmanyan, R., Shankar, N. U., & Chluba, J. 2016, AJ, 153, 26
Rao, M. S., Subrahmanyan, R., Shankar, N. U., & Chluba, J. 2017, ApJ, 840, 33
Reich, W. 1982, A&AS, 48, 219
Reich, P., & Reich, W. 1986, A&AS, 63, 205
Rubiño-Martín, J. A., Chluba, J., & Sunyaev, R. A. 2006, MNRAS, 371, 1939
Sathish, K., Saha, C., Sarkar, D., Siddiqui, J. Y., & Antar, Y. M. 2022, IAPM, 64, 82
Saurav, K., Sarkar, D., & Srivastava, K. V. 2015b, IAWPL, 14, 52
Saurav, K., Sarkar, D., Singh, A., & Srivastava, K. V. 2015a, ITAP, 63, 4286
Saurav, K., Sarkar, D., Singh, Y., & Srivastava, K. V. 2016, in Twenty Second National Conf. on Communication (NCC) (New York: IEEE), 1
Schaubert, D., Kollberg, E., Korzeniowski, T., et al. 1985, ITAP, 33, 1392
Shang, Y., Sun, J., Zhou, C., et al. 2023, IAWPL, 22, 1982
Singal, J., Haider, J., Ajello, M., et al. 2018, PASP, 130, 036001
Singh, S., Nambissan, Jishnu T, Subrahmanyan, Ravi, et al. 2022, NatAs, 6, 607
Subrahmanyan, R., Raghunathan, Agaram, Uday Shankar, N, et al. 2016, 2016 Int. Conf. on Electromagnetics in Advanced Applications (ICEAA) (New York: IEEE), 438
Subrahmanyan, R., & Cowsik, R. 2013, ApJ, 776, 42
Sunyaev, R., & Zeldovich, Y. B. 1970, Ap&SS, 7, 20
Sunyaev, R. A., & Chluba, J. 2009, AN, 330, 657
Switzer, E. R., & Liu, A. 2014, ApJ, 793, 102
Ta, S. X., & Park, I. 2017, RaSc, 52, 642
Ta, S. X., Park, I., & Ziolkowski, R. W. 2015, IAPM, 57, 107
Tauscher, K., Rapetti, D., & Burns, J. O. 2020, ApJ, 897, 175
Thyagarajan, N., Parsons, Aaron, DeBoer, David, et al. 2016, ApJ, 825, 9
Vernstrom, T., Scott, D., & Wall, J. 2011, MNRAS, 415, 3641
Vernstrom, T., Scott, D., Wall, J., et al. 2014, MNRAS, 440, 2791
Voytek, T. C., Natarajan, A., García, J. M. J., Peterson, J. B., & López-Cruz, O. 2014, ApJL, 782, L9
Wen, L.-H., Gao, S., Mao, C.-X., et al. 2018, IEEE Access, 6, 39725
Ye, L.-H., Liu, Gang, Jun Li, Yuan, et al. 2021, Int. J. RF Microw. Comput.-Aided Eng., 31, e22687
Ye, L. H., Zhang, X. Y., Gao, Y., & Xue, Q. 2020, ITAP, 68, 4428
Zannoni, M., Tartari, A., Gervasi, M., et al. 2008, ApJ, 688, 12